Materials and Design 202 (2021) 109550

Contents lists available at ScienceDirect

Materials and Design

journal homepage: www.elsevier.com/locate/matdes

Residual stresses in additively manufactured AlSi10Mg: Raman spectroscopy and X-ray diffraction analysis

Silvia Marola [a,b,*], Silvia Bosia [a,c], Alessandro Veltro [a], Gianluca Fiore [a], Diego Manfredi [b,c], Mariangela Lombardi [c], Giampiero Amato [d], Marcello Baricco [a], Livio Battezzati [a]

[a] Dipartimento di Chimica, Università di Torino, Via Pietro Giuria 7, 10125, Torino, Italy
[b] Istituto Italiano di Tecnologia (IIT), Center for Sustainable Future Technologies, Via Livorno 60, 10144, Torino, Italy
[c] Dipartimento di Scienza Applicata e Tecnologia (DISAT), Politecnico di Torino, Corso Duca degli Abruzzi 24, 10129, Torino, Italy
[d] Istituto Nazionale di Ricerca Metrologica (INRIM), Strada delle Cacce 91, 10135, Torino, Italy

HIGHLIGHTS

- Stress quantification on Si in AlSi10Mg by Laser Powder Bed Fusion using Raman and the modified Campbell and Fauchet model.
- Size of Si nano-crystals found with Raman modelling confirmed by TEM of extracted particles.
- Tensile stresses evidenced on the surface of additively manufactured samples while in-depth measurements indicate stress reversion in the bulk.
- Williamson-Hall method confirmed results of Raman and XRD and Eshelby's model provided stress transferred from Al to eutectic Si.

GRAPHICAL ABSTRACT

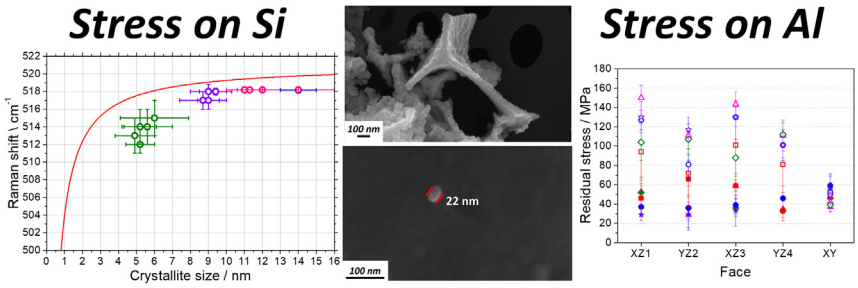

ARTICLE INFO

Article history:
Received 9 December 2020
Received in revised form 20 January 2021
Accepted 2 February 2021
Available online 04 February 2021

Keywords:
Residual stress
X-ray diffraction (XRD)
Raman spectroscopy
AlSi10Mg
Additive Manufacturing

ABSTRACT

Metal parts produced by Additive Manufacturing, and in particular Laser Powder Bed Fusion (LPBF), suffer from residual stresses due to high thermal gradients causing cyclic expansion and contraction of the alloy.
This work deals with the determination of residual stress in rapidly solidified AlSi10Mg samples using two non-destructive techniques: Raman spectroscopy, rapid, unconventional but applicable to Al—Si alloys, and XRD (ω-method), used as benchmark, being a classical method for determining residual stresses. Al stress level was studied by XRD both on the surface of LPBF samples and in the interior, after in-depth sectioning. Raman was employed to assess the stress on Si. The effect of particle size and stress on the Raman was separated determining the size distribution of Si particles, making Raman suitable to study residual stresses in alloys containing free Si.
Al and Si stresses were evaluated also by means of the Williamson-Hall method: stresses are of tensile type with agreement among all methods. Considering the alloy as a composite, stress on Si was estimated using the Eshelby's model, showing that larger eutectic particles undergo lower stress with respect to nanometric precipitates.

* Corresponding author at: Istituto Italiano di Tecnologia (IIT), Center for Sustainable Future Technologies, Via Livorno 60, 10144, Torino, Italy.
E-mail address: s.marola@unito.it (S. Marola).

https://doi.org/10.1016/j.matdes.2021.109550

1. Introduction

Additive Manufacturing (AM) processes by means of laser or electron beams imply the sequential melting of thin layers of alloy powders or wires on top of the same re-solidified material. Repeated local heating and cooling induce steep thermal gradients which are the main source of residual stresses in the as built part because of alternating thermal expansion and contraction of the alloy. Residual stresses, defined by UNI EN 15305:2008 as "*self-equilibrating internal stresses existing in a free body which has no external forces or constraints acting on its boundary*", can be classified according to the scale at which they occur. Stresses of type I vary over large distances, i.e. the dimension of the part, and can result in macroscopic deformation of components. Type II and type III stresses occur at the micro-scale due to the presence of different phases and lattice defects, respectively [1,2].

High residual stresses have detrimental effect on parts produced by AM leading to distortion, cracking, delamination, and change in mechanical properties of the alloy with respect to conventional processing. Their magnitude depends on the properties of the alloy and on the process parameters employed during the AM process. As reported for welding, they are highly non-uniform in space. To prevent the distortion of components, careful positioning of support structures is required, and job parameters should be optimized: laser power, scan speed, thickness of layers, scan vectors and part preheating to modulate the cooling rate and the consequent thermal gradients. Other key factors are thermal diffusivity, thermal expansion, yield stress, Young's modulus and melting point of the material being processed as well as the occurrence of metallurgical phenomena, e.g. phase transformations [2–4].

Studies on residual stresses in the various alloys employed in AM are available in the literature [1,5–27]. Techniques used for their determination were chosen by accounting for sampling volume, accuracy, and destructiveness, as well as the geometry of the component being built. Regarding Al alloys, usually processed through Laser Powder Bed Fusion (LPBF), residual stresses were determined experimentally using mainly neutron diffraction [14,21,26], X-Ray Diffraction (XRD) [10–13,17,19,20] and hole drilling [15,18].

Raman spectroscopy is known to provide information on microscopic strains in Si by analysing the shift of its transverse optical (TO) mode: blue shift is indicative of compressive stress while red shift is indicative of tensile stress as demonstrated for electronic grade Si and Si particles in cast Al alloys [28–36]. In the specific case of AM samples, the recovery of tensile stresses in Al—12Si has been shown by Li et al. [37] by following the position of the main Raman line of Si. The line was found at 517.6 cm^{-1} in the sample as built at a substrate temperature of 200°C whereas it occurred at the standard value of bulk Si, i.e. 523 cm^{-1}, in samples solution treated at 500°C for at least 1h [37]. Therefore, this technique appears suitable to determine quickly and non-destructively the stress level present in LPBF alloys containing free Si. However, the shift of the Raman peak is influenced also by the size of Si crystals, especially when the nanometre range is reached [38–49]. In their work, Campbell and Fauchet [50] explained that a distribution of tensile stresses in a Si sample produces a Raman shift similar to that resulting from a sample containing small Si crystals, however, in the latter case also broadening of the peak occurs. This is related to the fact that the optical properties of Si crystals change alongside with their dimension: in crystals of dimension less than 10 nm, quantum size and confinement effects become relevant, leading to a bandgap increase and to a modification of optical and electrical properties. Moreover, the finite space occupied by the nano-crystal limits the excitations of light scattering, because an uncertainty of the transferred wavevector $\vec{q}$ occurs with contribution from the whole Brillouin zone. This was investigated in porous Si samples, but never in alloys containing free Si particles.

In this work a systematic study of the residual stresses is performed in AlSi10Mg samples made by LPBF and by two other rapid solidification techniques, Copper Mould Casting (CMC) and Melt Spinning (MS), exhibiting different microstructures as demonstrated in a previous study [51], to check the effect of varying cooling rate on the Raman response. Conventional XRD ω-method is employed as benchmark for Al to investigate the stress level on different surfaces of LPBF samples. Raman spectroscopy accompanied by careful microstructural analysis was employed to evaluate the stress level of Si on the same surfaces analysed by XRD as well as in samples produced with CMC and MS and therefore with different cooling rates. The Raman shift found for the Si is first analysed accounting for the presence of both stress and size effects. Then, a correlation between stress found on Si and residual stress values obtained in the primary Al phase is sought using the Williamson-Hall method. Finally, assuming the alloy as a composite, the Eshelby's model is used to estimate the stress applied on Si by the Al primary phase.

2. Materials and methods

2.1. Sample synthesis

LPBF samples are cuboids of AlSi10Mg, 15x15x10 mm in size, built from gas atomised powders (purchased from EOS GmbH) with an EOSINT M270 Dual Mode equipment using 195 W laser power, 30 μm layer thickness, 800 mm/s scan speed, and 0.17 mm hatching distance [51] on a support of the same alloy which was finally removed. Scanning strategies were: i) scanning unidirectionally and rotating each layer of 67° (labelled 67), ii) scanning unidirectionally along the axis orthogonal to the recoater for the whole job (labelled X) [52]. The temperature of the building platform was kept at either 35°C or 100°C. One sample was produced without support on the building platform and was then removed by Electro Discharge Machining (EDM). LPBF samples were analysed both as built (AB) and after conventional stress relieving (SR) treatment (2h@300°C) on five of the six faces of cuboids labelled in Fig. 1. The bottom face was not considered because of its larger roughness due to support removal. For comparison, samples for residual stress investigation were produced using other rapid solidification techniques, i.e. CMC and MS, starting from the same AlSi10Mg gas atomised powders. Details on the production of CMC and MS samples were given in a previous study [51].

2.2. Sample characterization

Raman measurements were made on the five faces of LPBF indicated in Fig. 1 as well as on CMC cones, and MS ribbons acquiring spectra using a Renishaw Invia Raman Microscope coupled with a laser source of wavelength 442 nm applying power density of approximately 2.5 mW/μm^2 and accumulating 20 acquisitions of 5 s each. Samples were analysed on at least five random points on each surface and, in the case of MS ribbons, measurements were performed both on wheel and air side. Results from all points were then averaged.

XRD stress measurements were performed with a Panalytical X'Pert X-Ray using the K_α emission line of a Cu filament ($\lambda_{Cu} = 1.5418\ \AA$) as incident radiation, and focusing on the (422) reflection of the face centred cubic (fcc) Al-rich phase. The incident beam was focused using 5 mm and ¼° apertures, resulting in an irradiated area of approximately 14 mm^2.

XRD was performed at the centre of each face of the cuboid indicated in Fig. 1 both perpendicular (called *XY* direction) and parallel (*Z*-axis) to the building direction. On the top surface measurements were carried out in two perpendicular directions, denoted for simplicity *1* and *2*. The reference system for all measurements was established according to a label 3D-printed on the top of each cuboid, denoted as ID (Fig. 1). A list of the samples analysed together with the respective production parameters is reported in Table 1. The cuboids were analysed at first in their native form without any cutting or surface treatment; then

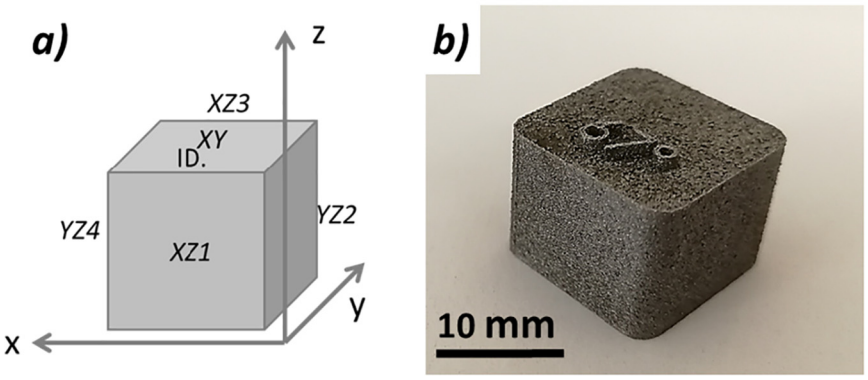

Fig. 1. Scheme of the cuboid sample with labels associated to all faces (a) and photograph of an as built cuboid detached from supports (b). ID. Marks the position of a label 3D printed on top of each cuboid identifying the scanning strategy employed for sample production and serving as reference.

Table 1
LPBF AlSi10Mg samples selected for residual stress measurements and processing parameters. The faces of the cuboids are labelled with a nomenclature (Fig. 1) added as a suffix after the sample name.

Sample name	Scanning strategy	Temperature of the building platform [°C]
AM_AB_67°_35°C	Rotation of 67°	35
AM_AB_67°_100°C	Rotation of 67°	100
AM_AB_X_35°C	Unidirectional X	35
AM_AB_X_100°C	Unidirectional X	100
AM_AB_67°_100°C_EDM	Rotation of 67°	100
AM_SR_67°_100°C	Rotation of 67°	100
AM_SR_X_35°C	Unidirectional X	35
AM_SR_X_100°C	Unidirectional X	100
AM_SR_67°_100°C_EDM	Rotation of 67°	35

in-depth measurements were performed along *Z*-axis at steps of 100 μm and on the *XY* face of the AM_AB_67°_100°C sample after electropolishing. Electropolishing was performed at 10 V for 30 s at room temperature employing as electrolyte a solution containing 90% ethanol and 10% perchloric acid (% in volume).

XRD patterns employed for the Williamson-Hall method were acquired using the same equipment in the 2θ range from 20° to 140° at steps of 0.0167°.

To investigate in deep the submicrometric and nanometric Si particles, FESEM micrographs were acquired with a ZEISS SUPRA TM 40 at 5 kV accelerating potential with 30 μm aperture, while TEM micrographs were acquired using a UHR-TEM by JEOL applying 300 kV accelerating potential.

2.3. Campbell and Fauchet model

Raman spectra were interpreted using a widely acknowledged confinement model proposed by Richter et al. [53] and extended by Campbell and Fauchet [50] for nano-crystals in porous Si. It considers that the lattice excitations due to light scattering are limited to the finite space of the crystal. Therefore, phonons are confined in the crystallite volume. For clarity, the Campbell and Fauchet model is summarized in the following. It considers a Stokes scattering event in an infinite crystal, in which the wavevector difference is transferred to a phonon with wavevector $\overrightarrow{q_0}$. The Bloch wave function of the generic phonon is composed by a $u\left(\overrightarrow{q_0},\vec{r}\right)$ function with the periodicity of the lattice multiplied by a plane wave, whereas, in the nano-crystal, the lattice term becomes $W\left(\vec{r},L\right)u\left(\overrightarrow{q_0},\vec{r}\right)$ with $W\left(\vec{r},L\right)$ as the phonon weighting function. The new wavefunction can then be written as $\Psi\left(\overrightarrow{q_0},\vec{r}\right)=\Psi'^{\left(\overrightarrow{q_0},\vec{r}\right)}u\left(\overrightarrow{q_0},\vec{r}\right)$, in which $\Psi'^{\left(\overrightarrow{q_0},\vec{r}\right)}$ is simply the product of the $W\left(\vec{r},L\right)$ and the plain wavefunction and can be expanded in a Fourier series having coefficients

$$C\left(\overrightarrow{q_0},\vec{r}\right)=\frac{1}{2\pi^3}\int d^3r\Psi\left(\overrightarrow{q_0},\vec{r}\right)e^{-i\overrightarrow{q_0}\vec{r}} \quad (1)$$

Assuming spherical Brillouin zone, neglecting scale factors, and assuming $\overrightarrow{q_0}$ for one phonon scattering, the Raman intensity can be written as a superposition of Lorentz curves with bandwidth γ centred at the theoretical wavenumber $\omega(q)$ of the phonon dispersion curve and weighted by the $\left|C\left(\overrightarrow{q_0},\vec{r}\right)\right|^2$ factor:

$$I(\omega)\propto\int d^3q\frac{\left|C\left(\overrightarrow{q_0}\right)\right|^2}{(\omega-\omega(q))^2-\left(\frac{\gamma}{2}\right)^2} \quad (2)$$

The integral is evaluated by means of a discrete summation that better accomplishes with the phonon quantization.

Through the well-known phonon dispersion relation, the wavelengths are easily calculated by considering the typical values of structural parameters of Si (Young modulus, lattice parameter of Si crystals, atomic mass). The wavevectors $\vec{q}$ can also be represented as discretised values of the phonon momentum, considering that allowed wavevectors will span the range $\frac{4.49}{L}, \frac{7.72}{L}, \frac{10.90}{L}, \ldots, \frac{2\pi}{a}$. This argument is the basis of the red shift of Raman feature when reducing nano-crystal size *L*, which represents the upper limit for the phonon wavelength: in other words, phonon wavelengths shorter than the lattice parameter can be considered in a reduced representation at the first Brillouin zone, while cannot exist if larger than the crystal size. It follows that the method can be applied to crystal dimension larger than a few lattice parameters, 1 nm is a typical lower limit while there is no upper limit, in principle. It must be noted, however, that the minimum wavevector is inversely proportional to *L*, then it saturates to zero for high *L*. The integration range of (2) does not vary anymore for $L > 10$ nm, as confirmed by the experimental evidence that both width and position of the phonon mode for crystallites is indistinguishable from that of bulk beyond that value. Several weighting functions (with corresponding Fourier coefficients) were proposed and tested in literature, but the Gaussian profile generally shows better agreement with experimental data [46,48,50,54]. The coefficients and the weighting function are hence defined as:

$$|C(0,q)|^2 \sim e^{\left(-\frac{q^2L^2}{16\pi^2}\right)} \; W(r,L) = e^{\left(-\frac{8\pi^2r^2}{L^2}\right)} \tag{3}$$

leading to broader and more shifted Raman peaks when nano-crystals are smaller.

This method was further expanded by Amato and Brunetto [48,54] by considering Si nano-crystals having log-normal distribution of size. In this way, L is no longer considered as a deterministic fitting parameter, but as a log-normal stochastic variable of size given by

$$dF(x) = \frac{1}{\sigma\sqrt{2\pi}}\, exp\left\{-\frac{[ln(x)-\chi]^2}{2\sigma^2}\right\} dln(x) \tag{4}$$

in which, $\chi = ln(x_0)$ is related to the most probable value of x which represents the dimension L of the nano-crystals. Two fitting parameters are used to reconstruct the Raman modes of the nano-crystals: χ, and the shape parameter, σ.

The analysis was carried out on the Raman spectra after subtraction of the baseline contribution. Mean squared errors were minimized by the Levenberg-Marquardt method, yielding the χ and σ values which define the corresponding size distribution.

2.4. Residual stresses by X-Ray diffraction

XRD stress measurements were performed using the ω-method both with negative and positive Ψ-offset following the UNI EN 15305:2008 and SAE HS-784:2003 standards. The value of residual stress, σ_ϕ, was calculated assuming plane stress conditions, i.e. that the component of stress normal to the sample surface is negligible, with the following equation

$$\varepsilon_{\phi\Psi} = \left(\frac{1+\nu}{E}\right)_{hkl} \sigma_\phi \sin^2\Psi - \left(\frac{\nu}{E}\right)_{hkl} (\sigma_1+\sigma_2) \tag{5}$$

in which $\varepsilon_{\phi\Psi}$ is the strain vector, ν is the Poisson ratio, E is the Young modulus, Ψ is the tilting angle selected for measurements, and σ_1 and σ_2 are biaxial stress components. If the stress is biaxial, the distribution of $d_{\phi\Psi}$ as a function of $sin^2\Psi$ has a linear trend [55]. The intercept of the straight line fitted to the experimental points gives the interplanar spacing at $\Psi = 0$

$$d_{\phi 0} = d_0\left[1-\left(\frac{\nu}{E}\right)_{hkl}(\sigma_1+\sigma_2)\right] \tag{6}$$

while the slope gives the residual stress in the specimen

$$\sigma_\phi = \left[\left(\frac{E}{1+\nu}\right)_{hkl} \frac{1}{d_0}\left(\frac{\partial d_{\phi\Psi}}{\partial \sin^2\Psi}\right)\right] \tag{7}$$

Intercept and slope values along with their errors were determined by means of linear regression imposing a 95% confidence level to the linear fit.

The elastic constants for the (hkl) plane under consideration were calculated with the Reuss approach (SAE HS-784:2003), that assumes all grains are subject to equal stresses. Instrument alignment was checked as suggested by the SAE HS-784:2003 and by the UNI EN 15305:2008 regulations by performing measurements on unstressed AlSi10Mg powders and on a superalloy specimen earlier employed in a round robin calibration test. The measurements at different Ψ angles were performed in the 2θ range from 135° to 141° with a step size of 0.0334° and collection time of 500 s at each position. The diffraction peaks were fitted with a pseudo-Voigt function using the X'Pert Highscore software by Panalytical to determine their position. Residual stress values, obtained at both positive and negative Ψ offset, were averaged to provide a mean stress value.

Stress values measured after in-depth sectioning were corrected accounting for the material removed following the procedure reported for flat plate in the SAE HS-784:2003 regulation. Calculations were performed considering the approximation applicable to shallow depths, since approximately 1% of the staring material was removed at each step.

2.5. Williamson-Hall method

The Williamson-Hall (WH) method is a simplified integral breadth method in which both size-induced and strain-induced broadening are determined by considering the peak width as a function of 2θ [56,57]. The WH formula employed for linear fitting of the data considering a confidence level of 95% for Al and of 80% for Si is

$$\beta_{hkl}\cos\theta = \frac{K\lambda}{D} + 4\varepsilon\sin\theta \tag{8}$$

with

$$\beta_{hkl} = \eta(\beta_{L\,\mathrm{exp}} - \beta_{instr}) + (1-\eta)\sqrt{\beta^2_{G\,\mathrm{exp}} - \beta^2_{instr}} \tag{9}$$

where D, the size of the scattering domains, and ε, the strain induced in the lattice, are obtained from the fit and β_{hkl} is the broadening of the reflection corrected for the instrumental broadening function, β_{instrt}, i.e. the broadening characteristic of the instrument employed for the analysis, K is a shape factor taken as 0.94, λ is the wavelength of the incident radiation, θ is the Bragg angle and η gives the fraction of Lorentzian contribution to the pseudo-Voight function. Employing these parameters, a plot in which 4sinθ represents the x-axis and β_{hkl}cosθ the y-axis is drawn, and from the intercept and from the slope of the linear fit of the data the size of the scattering domains and the lattice strain are computed, respectively.

All reflection profiles in the diffraction pattern were fitted analytically to determine the peak position, the full width at half maximum and Lorentzian contribution to peak shape [58]. Linear fitting of the data was performed considering a confidence level of 95%.

3. Results and discussion

3.1. Micro-stress using Raman spectroscopy

A set of measurements by Raman spectroscopy was performed on the AlSi10Mg samples produced by means of different rapid solidification techniques spanning a large range of cooling rates. From a previous study [51] with similar samples, it was determined that the eutectic fraction changes steadily in the order CMC > LPBF ~ MS (air side) together with the length scale of the microstructure which is constituted by cells or columns of primary Al and fine fibrous eutectic in LPBF samples, while it is less refined in MS and coarser in CMC samples. It was shown that these samples contain also precipitates of various size in the Al matrix. They were formed after solidification of the Al matrix supersaturated with Si due to the self-heating effect of recalescence. The Si precipitates are of nanometric size in the LPFB samples.

Fig. 2 shows the comparison of the TO mode of Si crystals contained in samples produced by CMC, MS, and LPBF before and after SR, together with a reference spectrum of large-grained polycrystalline Si with no internal stress. Increasing the cooling rate, i.e. from the CMC to MS and to AB LPBF samples, the Raman signal is red shifted and broadened (Fig. 2). After the SR treatment, the Raman peak of the LPBF sample is shifted back towards the position of the reference and is narrower with respect to the sample in AB condition. The shifts shown in Fig. 2 are indicative of the effect rapid solidification on the AlSi10Mg alloy. However, it is well-known that the Raman signal of Si is more affected by crystals of nanometric size than by micrometric ones. This is related to the fact that the Raman cross section of the Si nanostructures is larger than in

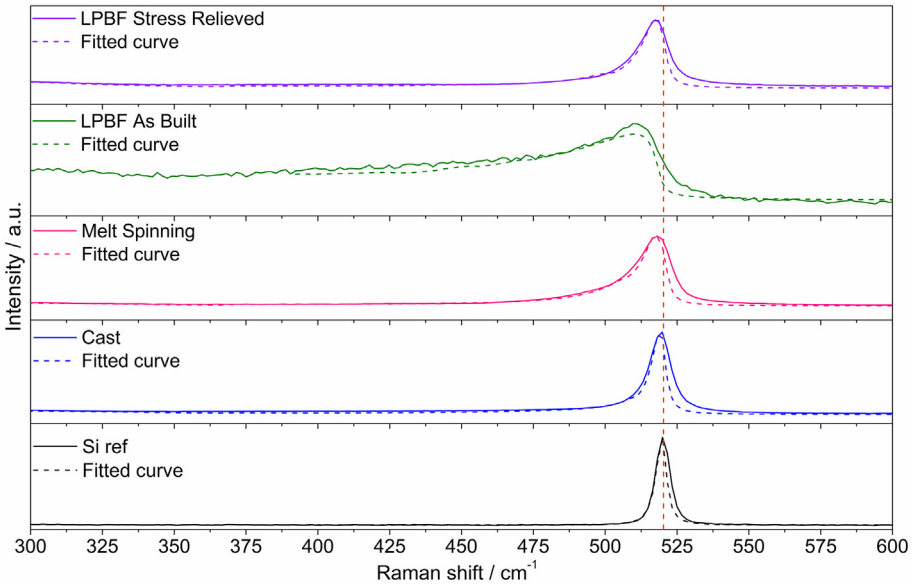

Fig. 2. Raman spectra acquired on AlSi10Mg samples produced by means of different rapid solidification techniques (full line), along with the fit of the signal obtained after the analysis with the modified Campbell and Fauchet model (dashed line). From bottom to top: polycrystalline Si, AlSi10Mg produced by casting (CMC), melt spinning (MS) and LPBF before and after stress relieving treatment. The red dashed line represents the position of the Si transverse optic mode in absence of stress and nano-crystals. (For interpretation of the references to colour in this figure legend, the reader is referred to the web version of this article.)

bulk Si due to the different phonon density of states. This allows to interpret the small discrepancy between the experimental data and the fit in the right-hand tail of spectra in Fig. 2 as the residual contribution of larger (>10 nm) structures.

To separate the effect of size and stress, an experimentally determined correlation between size of Si nano-crystals and Raman shift reported by Ossadnik et al. [43] is used as shown in Fig. 3. The peak position and dimension of Si nano-crystals obtained by means of the present fitting of spectra for all samples produced by means of different rapid solidification techniques and the LPBF samples produced with different process parameters follow the general trend described in [43], but the points are all shifted to lower wavenumber. Samples produced by CMC (blue), MS (pink) and LPBF plus SR treatment (violet) have larger Si crystals and lower Raman shift, while samples produced by LPBF in the AB condition (green) have smaller crystals and display larger red shift. Since the LPBF samples contain both eutectic Si and fine precipitates [41], it is apparent that only the fine crystals contribute to determine the position, shape and intensity of the Raman lines. The displacement of the points with respect to the reference curve indicates the presence of tensile stress contributing to the shift of the Raman signal. The experimental curve from Ossadnik et al. [43] confirms the arguments in section 2.3 about the size range for validity of the model used

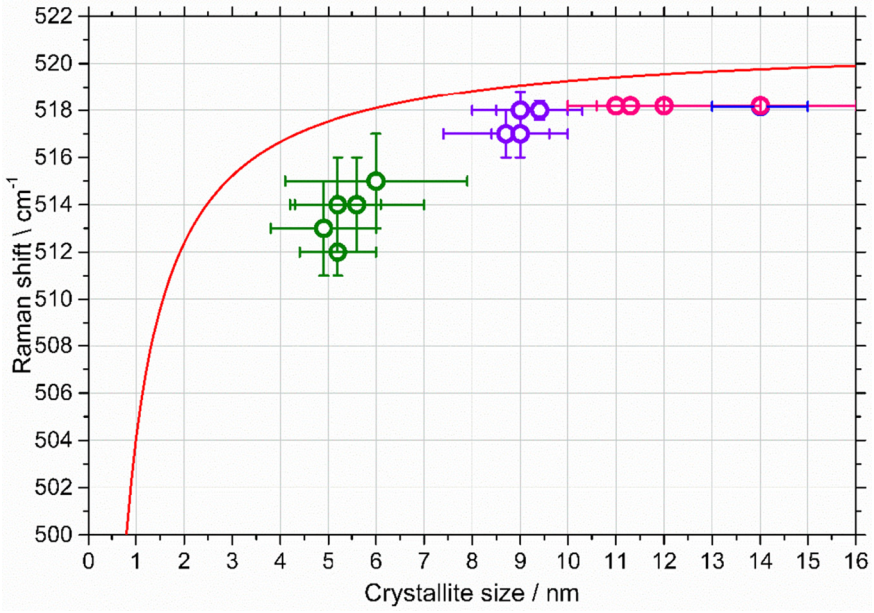

Fig. 3. Comparison of the Si dimension obtained with the Campbell and Fauchet model applied to samples produced by CMC (blue), MS (pink) and LPBF both before (green) and after (violet) the stress relieving treatment. In samples produced by LPBF the error bars represent the average of the results obtained on the different faces of the analysed cuboids. The full red line represents the experimentally determined relationship described by Ossadnik et al. in [43].

for interpreting Raman data. Si in eutectic shows domains with dimension ranging beyond the upper limit of the model, then its contribution does not affect the shape of the modes depicted in Fig. 2.

The results of measurements on the LPBF samples produced varying the scanning strategy and the temperature of the building platform both in AB and SR conditions, already contained in Fig. 3, are explained in detailed in ***Fig. S2*** (in Supplementary Information). It shows that the position of the peak has limited variability indicating that the different process parameters employed here had limited influence on Si dimension and on the stress level of samples. However, it is underlined that the model discriminates between samples in AB condition, having average Si dimension around 5 nm, and SR samples, having Si dimension in the range 7÷11 nm.

The present findings extend the information gathered by Raman analysis with respect to that reported by Li et al. [37] using samples built with a substrate temperature of 200°C. Therefore, the inherent annealing must have caused precipitation and growth of Si in the Al matrix. In fact, previous Differential Scanning Calorimetry experiments at the heating rate of 20 K/min [51] have shown that Si precipitation from supersaturated Al starts at about 170°C already. It could be assumed that during the production of the samples employed by Li et al., Si must have grown above the approximate limit of 10 nm reducing the effect of size on the position of the Raman line.

To validate the results on the dimension of Si crystals by direct observation, a portion of the AB alloy was treated with diluted HCl solution to dissolve selectively the Al leaving the Si unetched [59]. Dissolution took several days at approximately 70°C. Once it was completed, the resulting suspension and deposit were filtered with medical dialysis membranes (D9777 by Sigma Aldrich having molecular weight cut-off approximately of 14′000) to retain the Si particles including nanometric precipitates. Both the filtrate and bulk AB samples were observed with FESEM and TEM to compare the dimensions of Si particles (Fig. 4).

Fig. 4-***a*** and ***4-c*** show examples of fibrous eutectic Si which forms a shell around the Al cells. It appears composed of aggregated particles, having dimensions below 50 nm. They form thick layers joining at triple points, in a sort of complex 3D shape. This morphology is newly revealed with respect to that observed in conventional micrographs, e.g. Fig. 4-***b*** and ***4-d***. Here, continuous layers of fibrous eutectic (darker

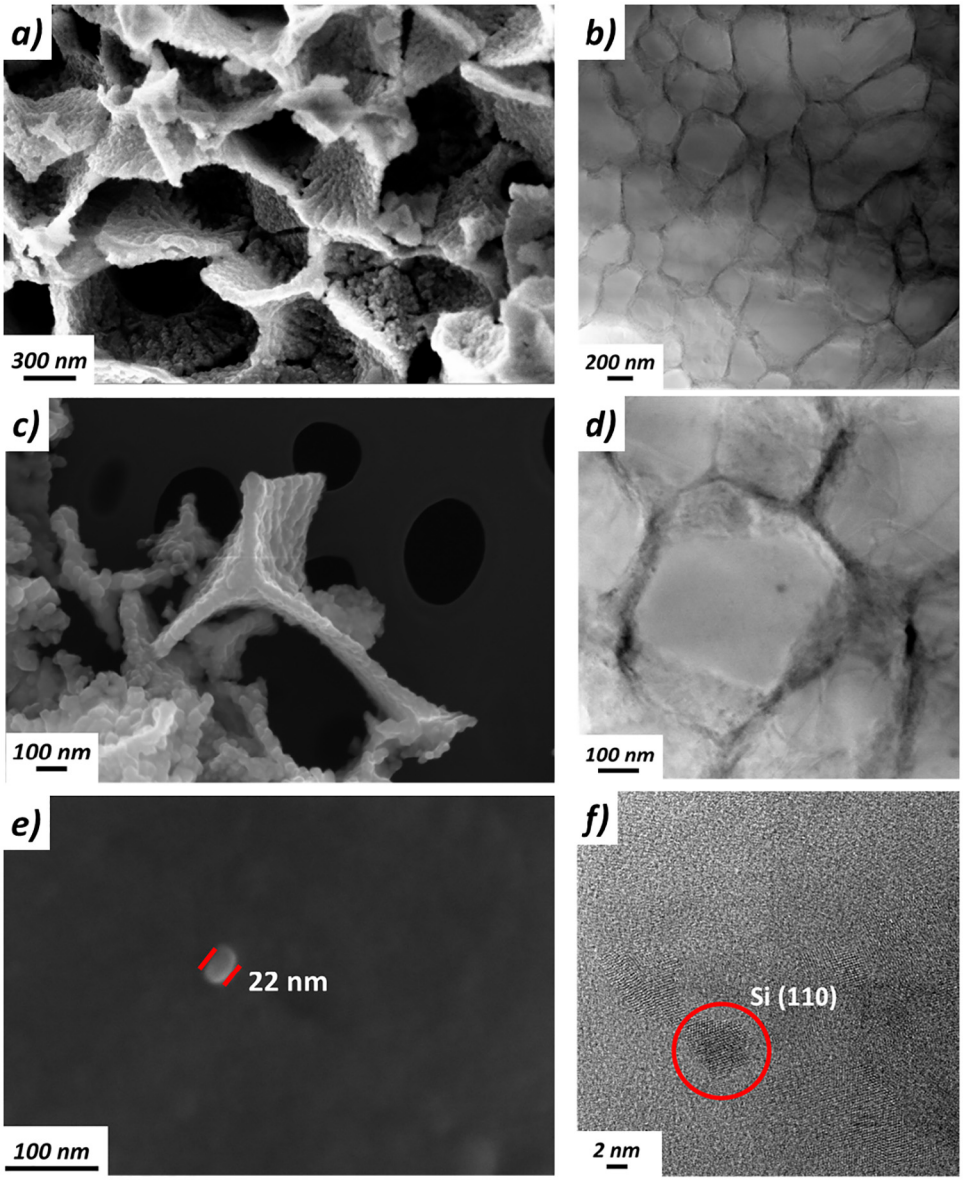

Fig. 4. FESEM images of the Si extracted from LPBF samples (left) and TEM images of an LPBF sample (right). In detail: (a) and (b) are low magnification images in which is shown the 3D shape of eutectic Si; (c) and (d) show an isolated eutectic Si fiber; while (e) and (f) represent Si precipitates either loose (e) or embedded in the matrix (f).

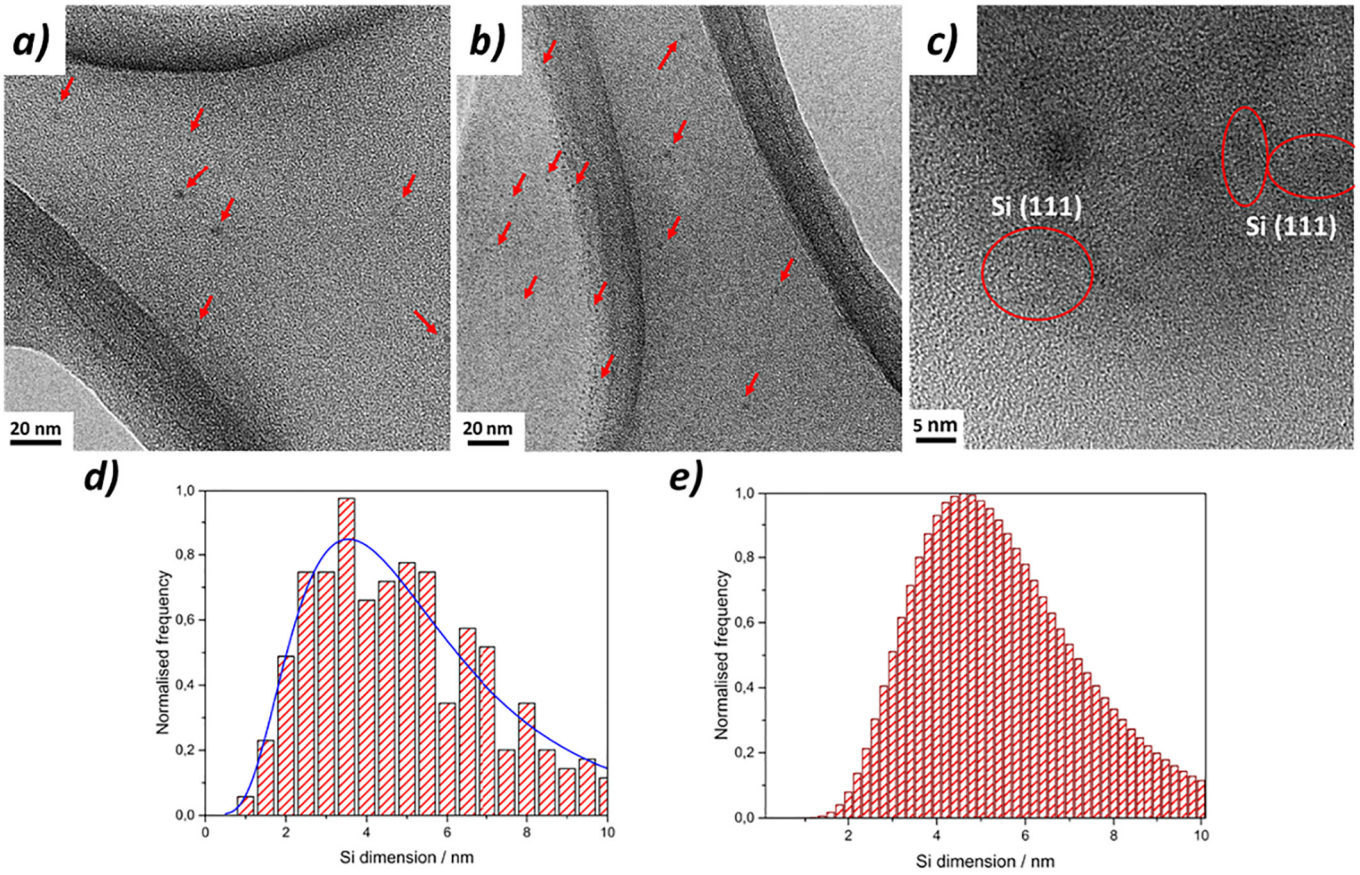

Fig. 5. TEM micrographs representing the nanometric Si crystals removed from the α-Al matrix (a) and (b), along with a high-resolution micrograph in which it is possible to identify the lattice fringes of (111) Si crystals, (c). Comparison of the distribution of Si dimensions determined by TEM analysis (d) and applying the modified Campbell and Fauchet model to Raman spectra (e). The blue line in (d) represent the lognormal fit of the experimental data. (For interpretation of the references to colour in this figure legend, the reader is referred to the web version of this article.)

grey) surrounding the Al matrix (lighter grey) can only be seen. In further FESEM images, close to the instrumental limit, isolated nano-crystalline Si particles were evidenced having dimensions around 20 nm (Fig. 4-***e***) which, however, are not small enough to contribute significantly to the Raman shift described earlier.

Further TEM analyses performed both with bulk samples and the Si extracted from the Al matrix showed finer Si features. Precipitates were imaged in the Al matrix (Fig. 4-***f***) having diameter of approximately 5 nm displaying lattice fringes compatible with those of (110) planes of Si. Their size corresponds to that found by analysing the Raman spectra and is fully in agreement with what reported recently by Qin et al. [60] who studied in detail the shape and structure of Si nano-crystals which reasonably occur in the present sample as well.

A further proof of the presence of nanometric Si was obtained by observing the finest part of the Si extracted from the Al matrix with TEM. Fig. 5 reports images displaying the Si nano-crystals dispersed on the carbon grid which holds the sample (Fig. 5-***a*** and ***5-b***). EDX analysis and measurements of the interplanar spacing from the lattice fringes at high resolution (Fig. 5-***c***) confirmed that the particles are Si crystals. In TEM observations Si crystals appeared mostly spherical or elliptical in shape, again completely in accordance with the findings by Qin et al. [60]. The distribution of the dimension of Si nano-crystals extracted from the LPBF sample was determined after observing about 300 particles. It is compared with one of the several similar distributions obtained by applying the modified Campbell and Fauchet model in Fig. 5-***d*** and ***5-e*** which shows good agreement between the two distributions. Therefore, it can be stated that the Raman shift is due both to size effect as suggested by the experimental work on pure Si [43], and to the presence of a tensile stress on the surfaces of all the present samples subjected to rapid solidification.

After that, the local stress on Si for the different rapidly solidified samples was evaluated by subtracting the contribution of the shift due to the size of Si crystals as obtained by means of Raman spectroscopy. The following relationship was employed as a first approximation,

$$\sigma = \Delta\omega \cdot 250\ MPa \tag{10}$$

which was applied to Si in electronic devices in the presence of isotropic biaxial stress [29].

The average results obtained for all samples are reported in Table 2 along with the strain determined using the Young modulus of Si (140 GPa). The stress on Si in the LPBF AB sample is much higher than in any other one even considering the large scatter. The Si fine particles in CMC, MS, and LPBF SR samples appear to be similarly stressed, possibly because of a shear lag effect imposed by the Al matrix on precipitates.

Table 2
Quantification through Raman spectroscopy of local micro-stress and strain of Si in AlSi10Mg samples by different rapid solidification techniques. The scatter provided corresponds to one standard deviation.

	CMC	MS	AM_AB	AM_SR
σ_{Si} [MPa]	402 ± 25	341 ± 38	1038 ± 243	392 ± 134
ε_{Si}	0.0029 ± 0.0002	0.0024 ± 0.0003	0.007 ± 0.002	0.03 0.001

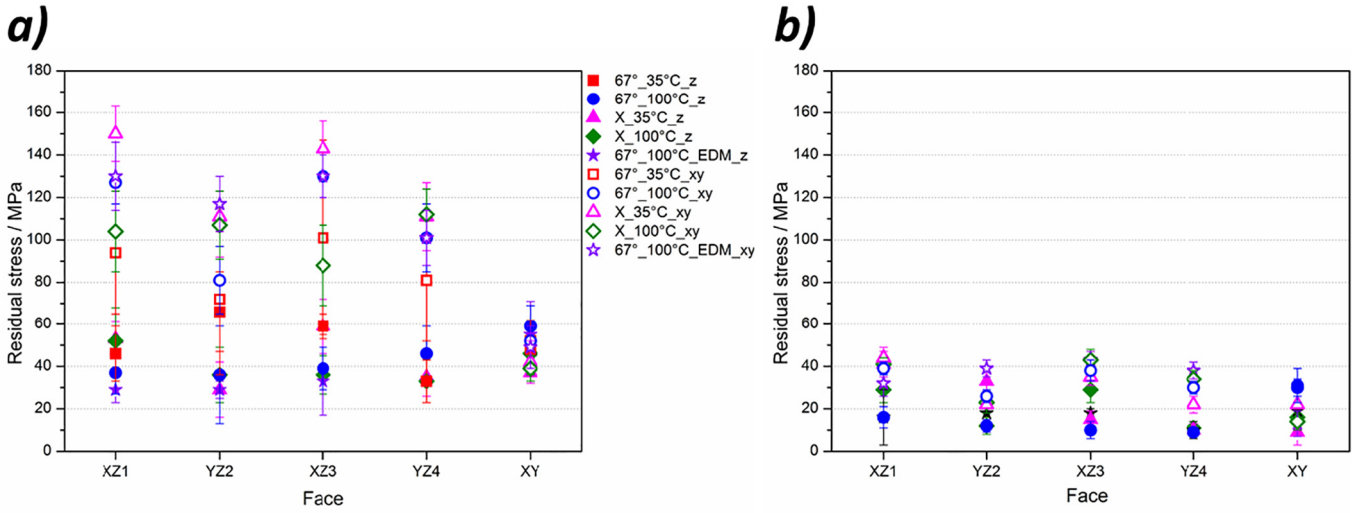

Fig. 6. Comparison of the stress values obtained both perpendicularly (XY/2) and parallel (Z/1) to the building direction for each face of the LPBF samples in the AB conditions (a) and after the stress relieving treatment (b).

3.2. Macro-stress using X-Ray Diffraction

It is well established that the information on residual stress in samples analysed by XRD depends on the penetration depth of X-rays in the material, i.e. in AlSi10Mg a region comprised in between 20 μm and 40 μm below the surface, as reported in UNI EN 15305:2008 and SAE HS-784:2003 standards.

The measurements performed on the upper *XY* face of the LPBF sample in AB condition suggest that the stress remains constant within the scatter in both directions of analyses (*1* or *2*) (Fig. 6-***a***). For the lateral faces of the cuboids, a clear distinction in stress results is found along the *XY* (higher stress) and *Z* (lower stress) directions, all stresses being tensile (Fig. 6-***a***). This is explained considering that during the LPBF process there is strong directionality in heat flow along the building direction (*Z*-axis) causing stress development with a preferential orientation in the cuboids whereas the heat flow from the external upper surface is homogeneous in space. The stress values found experimentally are of the same order of magnitude of those reported in literature with several techniques [7,12,14,15,17,19,20]. This result correlates well with the microstructure of AlSi10Mg processed by means of LPBF. In fact, it is well known that the Al grains are mostly columnar along the building direction and equiaxed in the perpendicular direction [61–64], as verified for a sample of the present study by EBSD (maps given in ***Fig. S3*** of Supplementary Information). Therefore, the different stress level found in the two directions is associated to the different amount of grain boundaries sampled in each XRD measurement. The constant stress values obtained in the *1* and *2* directions of the top surface of the cuboids is in accordance with the occurrence of equiaxed Al grains.

After the SR treatment the tensile residual stress decreased to about 30 MPa with close values in all annealed samples for all directions of

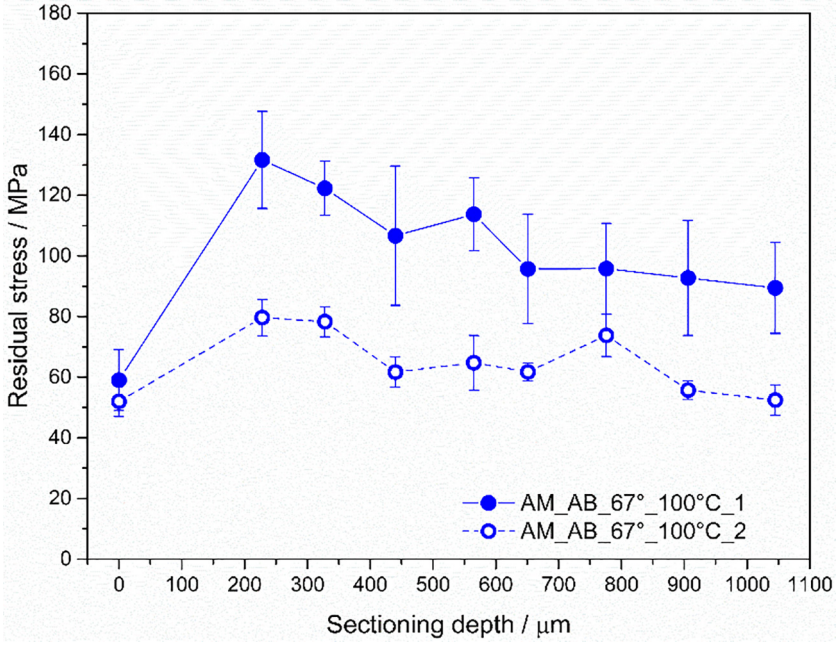

Fig. 7. Determination of the stress level of the LPBF AB sample (with rotation of 67° and building platform temperature 100°C) moving from the XY face of the cuboid towards its centre at steps of approximately 100 μm (blue). (For interpretation of the references to colour in this figure legend, the reader is referred to the web version of this article.)

analysis within the scatter of results (Fig. 6-***b***). This corresponds to the microstructure reported in the literature [65,66], where it is demonstrated that after SR columnar grains tend to become more equiaxed. From this first set of results it is possible to state that, in this case, the differences in scanning strategy and temperature of the building platform employed in this work do not affect appreciably the stress level present in both samples built with and without supports.

On the other hand, the literature reports results of in-depth stress determination by hole-drilling [15,18] which indicated an oscillating trend of residual stresses over distances of fraction of millimetres reaching in some place values well above the yield strength of the alloy, which represents a limit for the quantitative use of the technique. To verify the amount of stress in the core of the present AB sample, XRD measurements were carried out along both the *1* and *2* direction after removing material at steps of approximately 100 μm. The main laser processing parameters of the outer top skin perpendicular to the building direction, which correspond to two-layers thickness, were slightly different from the core ones, consisting of a laser power of 120 W, a scan speed of 900 mm/s and a hatch distance of 0.10 mm [51]. After a first increase in stress when moving from the contour, i.e. the zero point of penetration, to the core of the sample starting at about 200 μm (Fig. 7), the stress level was found to decrease slightly for all steps of material removal. This result seems to indicate that part of the tensile stress is released when moving towards the interior of the cuboid. This is in accordance with literature [1,4,8,16], in which it is stated that compressive stresses are found in the core of additively manufactured samples. Moreover, a difference is observed in the tensile stress state of the sample along the *1* and *2* perpendicular directions for all the sectioning steps. This difference in stress is in accordance with what suggested by the EBSD map of the *XY* face (***Fig. S3-a*** of the Supplementary Information), where grains appeared slightly elongated along direction *2*, and by reference [8] which states that generally on the *XY* surface the stress along the laser tracks is higher with respect to that measured perpendicularly to them. Differences in stress, moreover, were reported in [19,20] when analysing different portions of the same samples suggesting that stress could be related also to the position and the orientation of the sample on the building platform.

3.3. Correlation of results obtained by Raman and XRD techniques

Both Raman and XRD suggested the presence of tensile residual stress on the surface of rapidly solidified samples, especially those produced by LPBF in AB condition. The Raman spectroscopy, though, refers to the stress experienced by Si nano-crystals in the alloy, while the stress determined by XRD refers to the macro-stress acting on the Al matrix.

The possible correlation between stresses measured with the two techniques needs to be discussed. This is done at first by applying the WH method for the determination of strain of both Al and Si from the full XRD patterns acquired on the rapidly solidified AlSi10Mg samples produced by means of different rapid solidification techniques, i.e. CMC, MS ribbons (both on air and wheel side) and the internal surface

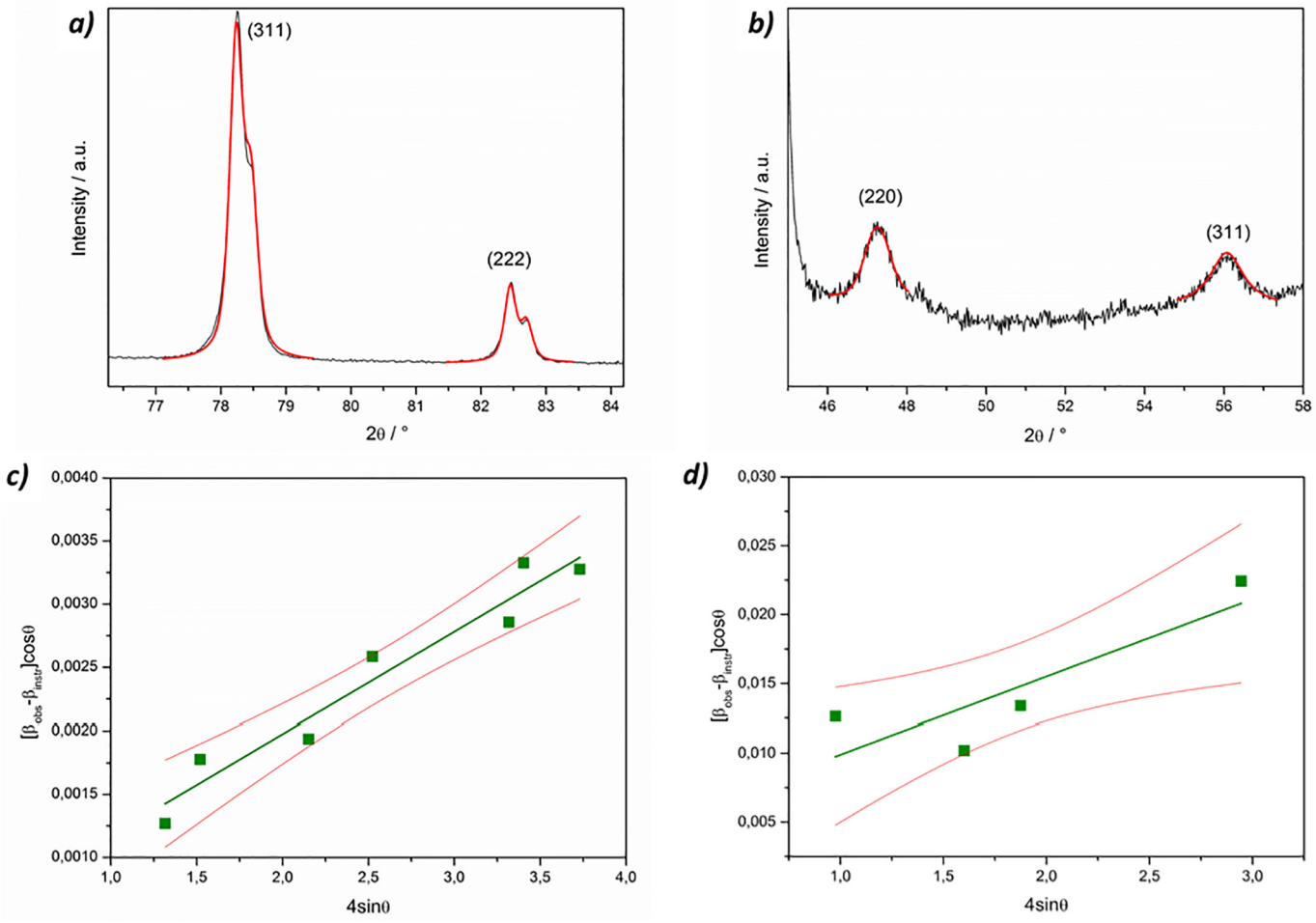

Fig. 8. Examples of reflections of Al and Si phases with the respective fitting and WH plots obtained for the LPBF AB sample (with rotation of 67° and building platform temperature 100°C). (a) and (c) show peak fitting and WH plot for Al reflections, respectively; (b) and (d) show those for Si reflections. Red lines in (c) and (d) provide the confidence bands used in the fitting. (For interpretation of the references to colour in this figure legend, the reader is referred to the web version of this article.)

Table 3
Results of the WH analysis performed with the Al reflections.

	D_{Al} [nm]	$<\varepsilon_{Al}^2>^{1/2}$	σ_{Al} [MPa]
CMC	290 ± 348	0.0003 ± 0.0002	21 ± 14
MS	188 ± 191	0.0003 ± 0.0002	20 ± 12
AM_AB	362 ± 543	0.0008 ± 0.0002	56 ± 14
AM_SR	–	–	–

Table 4
Results of the WH analysis performed with the Si reflections.

	D_{Si} [nm]	$<\varepsilon_{Si}^2>^{1/2}$	σ_{Si} [MPa]
CMC	145 ± 290	0.003 ± 0.001	434 ± 140
MS	124 ± 285	0.0031 ± 0.0007	427 ± 102
AM_AB	36 ± 81	0.006 ± 0.004	840 ± 560
AM_SR	241 ± 362	0.0018 ± 0.0003	252 ± 42

of LPBF cuboids, both AB and SR. Then, a comparison with a model established for composites containing two phases is made.

3.3.1 Williamson-Hall method

An example of the XRD reflections of both Al and Si, the respective fit, and the resulting WH plots is reported in Fig. 8. The resulting strain obtained from the application of the model, along with stress levels in the crystals obtained by multiplying the strain for the Young modulus of the elements (70 GPa for Al and 140 GPa for Si [67]) are reported in Table 3 and Table 4, respectively. From these results it is apparent that the determination of the size of scattering domains, *D*, comes with a large error for most samples, while the determination of stress is generally more precise. The uncertainty in the determination of the dimension of the scattering domains is related to the fact that both Al and Si crystals which give the maximum intensity to reflections in these samples are considerably large with respect to those typically considered by the WH method; for this reason, when performing the linear regression, the intercept falls close to zero (corresponding to infinite size of scattering domains). In the case of the WH plot performed for Al reflections of the SR sample the intercept value is negative and for this reason no results were reported for this sample.

Nevertheless, in the case of Si the hierarchy of Si crystals dimensions found in the micrographs is reproduced. It is noted, on the contrary, that the strain is provided by the breath of the reflections which is caused by the finer particles.

The stress level obtained for Al in the LPBF AB sample agrees well with that obtained from the determination performed using the XRD ω-method. It is always lower with respect to the levels obtained for Si which are of the same order of magnitude as those reported in Table 2 resulting from Raman spectroscopy. Results for the LPBF AB sample come with a large error bar because only four Si reflections in the XRD patterns have enough intensity to be fitted with confidence. This is due to the fine size of precipitates and to the reduced amount of free Si due to the extension of solid solubility of Si in Al both achieved with the high cooling rate involved in LPBF [41].[1] However, the results obtained by applying the WH method appear useful in correlating the stress determined by conventional XRD and that obtained by Raman and suggest that all the Si, large eutectic particles and fine precipitates, are subject to stresses. Moreover, the higher stress level obtained for Si agrees with the report by Kim et al. [26] stating that a large amount of stress is concentrated on Si in Al—Si alloys where, also the fracture strength of large grained eutectic Si is reported to be as high as 1 GPa [30,31]. The values obtained with the Williamson-Hall method agree with these literature results.

3.3.2 Transfer of stress from the Al matrix to Si: Comparison with composites

Since stresses in two phase materials have been amply discussed in the literature concerning composites, a simplified Eshelby analysis for the transmission of stress from matrix to reinforcement particles in composites [30,68] is performed starting from results on residual stress determined on Al by means of XRD.

In dealing with the cast Al—Si system, Harris et al. [30] suggest that it is possible to estimate the tensile stress in the elastic regime of deformation of particles, here the minority Si, when knowing the tensile strain applied to the composite, by using the Eshelby's analysis for pure shear case. The model gives the tensile stress acting on the reinforcement particles, σ_p, as:

$$\sigma_p = EK\varepsilon_c \tag{11}$$

in which

$$K = \frac{1+(1-f)\gamma M}{1-fM} \quad \gamma = \frac{7-5\nu}{15(1-\nu)} \quad M = \frac{\left(\frac{\mu^*}{\mu}-1\right)}{\left(\frac{\mu^*}{\mu}-1\right)\{1-\gamma(1-f)\}+1} \tag{12}$$

where *E* and ν are the Young modulus and Poisson ratio of the matrix (70 GPa and 0.33 for Al), respectively, ε_c stands for the applied tensile strain on the composite, *f* is the overall volume fraction of reinforcement, and μ and μ^* are the shear moduli of matrix (24.81 GPa for Al [30]) and reinforcing agent (66.41 GPa for Si [30]), respectively. Here, the applied tensile strain used for the determination of the stress in particles was taken as the stress determined on Al by XRD, while the overall volume fraction was taken as the amount of Si present in the alloy under investigation.

Results on Si residual stress obtained by applying the model for the case of AB LPBF samples span from 56 to 79 MPa along *Z* and from 126 to 175 MPa along *XY*, with errors consistent with these ranges in both directions. Results obtained on SR samples span from 25 to 34 MPa along *Z* and from 46 to 52 MPa along *XY*, again with errors that span the values range. The stresses obtained for each sample are reported in ***Table S2*** and ***Table S3*** in Supplementary Information. All stresses on Si calculated by applying this model considerably differ with respect to those obtained by means of Raman spectroscopy and WH analysis. The difference is explained by the effect of the dimension of Si crystals in the determination of the stress. In both Raman and WH methods the results are mostly influenced by the nanometric Si crystals, while the model for reinforcing particles in composites was developed for crystals of larger size. Therefore, the two results describe the different stress level experienced by larger (eutectic Si) and smaller (Si precipitates) crystals. Another factor that could explain the high stress level observed for the nanometric Si particles is that they appear to be coherent with the surrounding matrix and, therefore, are bearing a coherency stress, as observed by Qin et al. [60]. From these results it seems that the stress derived from the Harris's model represents the actual one transferred by the Al matrix to the Si crystals, due to the thermal stresses arising during the process; while the higher values obtained with the other two techniques account also for the presence of coherency with the matrix of the nano-crystals increasing the stress level at the nanometric scale.

4. Conclusions

The determination of residual stresses in AlSi10Mg samples produced by LPBF AB and after SR, and by the rapid solidification

[1] It should be noted that on etching away the Al, the Si would de-alloy and likely cluster in small solid particles or diffuse to existing crystals thereupon the size distribution would deviate somehow from the original one in the AB sample.

techniques CMC and MS, was carried out using Raman spectroscopy and XRD diffraction.

Considering Raman results, it was found that increasing the cooling rate, from CMC to MS and to LPBF, would correspond to a red shift and to a broadening for the peak of free Si. For LPBF samples after SR the signal was shifted back close to the position for bulk Si. The shift was found to be related both to the presence of residual stresses and Si nano-crystals. To discriminate between these two contributions, the modified Campbell and Fauchet model was applied to evaluate the size distribution of Si nano-crystals in the samples. The presence of Si nano-crystals in the Al matrix of LPBF AB samples was verified analysing the Si extracted from the alloy trough a TEM. Finally, it was deduced that all rapidly solidified samples have a red shift caused by tensile stresses.

Considering XRD, stress measurements on both LPBF AB and SR cuboids showed different stress levels on Al according to the direction of the measurement on the lateral faces, the one perpendicular to the building direction being higher. This discrepancy was explained considering the differences in Al grain size observed by EBSD. The lower stress value along the building direction with respect to the perpendicular direction was related to the lower amount of Al grain boundaries encountered during the XRD measurements. On the top face of cuboids, the same stress along the two perpendicular directions was found, in agreement with the equiaxic nature of Al grains. After SR the level of residual stress decreased, confirming the validity of such thermal treatment. Moreover, from the evaluation of the stress in-depth, moving from the contour to the core of the cuboid at steps of approximately 100 μm, it was found that the value of stress decreased slightly when increasing the sectioning depth.

It can be concluded that the stress found with Raman spectroscopy refers to the micro-stress acting on the fine Si precipitates, while the stress determined by XRD refers to the macro-stress acting on the Al matrix. Finally, the correlation between these results was investigated by means of the WH analysis of full XRD patterns and by applying a simplified Eshelby's model. The WH analysis provided results on stress which turned out of the same order of magnitude of that determined on Al by XRD and on Si by Raman validating the use of these techniques to determine the stress in rapidly solidified AlSi10Mg samples. On the other hand, the simplified Eshelby's model provided stress values considerably lower than those obtained by both Raman and WH. This appears related to the different Si dimensions in the samples, i.e. Si precipitates determining the Raman and WH results and eutectic Si determining the outcome of the Eshelby's approach.

Overall, this work provides a clear distinction among the stresses occurring in LPBF samples of AlSi10Mg and a detailed working procedure to determine residual stresses in alloys containing free Si.

Declaration of Competing Interest

The authors declare that they have no known competing financial interests or personal relationships that could have appeared to influence the work reported in this paper.

Acknowledgements

This work was supported by Regione Piemonte through project STAMP (Sviluppo Tecnologico dell'Additive Manufacturing in Piemonte). Dr. Enrica Bosco of GE-Avio, Rivalta (TO), Italy, is kindly acknowledged for providing the test sample employed to verify the alignment of the diffractometer.

Data availability

The raw/processed data required to reproduce these findings cannot be shared at this time due to technical or time limitations.

Author Statement

Silvia Marola: Conceptualization, Data curation, Formal analysis, Investigation, Methodology, Validation, Visualization, Writing – Original draft preparation **Silvia Bosia:** Data curation, Formal analysis, Investigation **Alessandro Veltro:** Data curation, Formal analysis, Investigation, Software **Gianluca Fiore:** Methodology, Validation **Diego Manfredi:** Resources, Writing – Reviewing & Editing **Mariangela Lombardi:** Funding acquisition, Writing – Reviewing & Editing **Giampiero Amato:** Methodology, Software, Supervision, Writing – Reviewing & Editing **Marcello Baricco:** Supervision, Writing – Reviewing & Editing **Livio Battezzati:** Conceptualization, Funding acquisition, Supervision, Writing – Reviewing & Editing.

Appendix A. Supplementary data

Supplementary data to this article can be found online at https://doi.org/10.1016/j.matdes.2021.109550.

References

[1] P. Mercelis, J. Kruth, Residual stresses in selective laser sintering and selective laser melting, Rapid Prototyp. J. 12 (2006) 254–265, https://doi.org/10.1108/13552540610707013.

[2] N.S. Rossini, M. Dassisti, K.Y. Benyounis, A.G. Olabi, Methods of measuring residual stresses in components, Mater. Des. 35 (2012) 572–588, https://doi.org/10.1016/j.matdes.2011.08.022.

[3] T. DebRoy, H.L. Wei, J.S. Zuback, T. Mukherjee, J.W. Elmer, J.O. Milewski, A.M. Beese, A. Wilson-Heid, A. De, W. Zhang, Additive manufacturing of metallic components – process, structure and properties, Prog. Mater. Sci. 92 (2018) 112–224, https://doi.org/10.1016/j.pmatsci.2017.10.001.

[4] Z.C. Fang, Z.L. Wu, C.G. Huang, C.W. Wu, Review on residual stress in selective laser melting additive manufacturing of alloy parts, Opt. Laser Technol. 129 (2020) 106283, https://doi.org/10.1016/j.optlastec.2020.106283.

[5] M. Shiomi, K. Osakada, K. Nakamura, T. Yamashita, F. Abe, Residual stress within metallic model made by selective laser melting process, CIRP Ann. - Manuf. Technol. 53 (2004) 195–198, https://doi.org/10.1016/S0007-8506(07)60677-5.

[6] C. Meier, R.W. Penny, Y. Zou, J.S. Gibbs, A.J. Hart, Thermophysical Phenomena in Metal Additive Manufacturing by Selective Laser Melting: Fundamentals, Modeling, Simulation and Experimentation, Annu. Rev. Heat Transf, 2017 http://arxiv.org/abs/1709.09510.

[7] J. Wu, L. Wang, X. An, Numerical analysis of residual stress evolution of AlSi10Mg manufactured by selective laser melting, Optik (Stuttg). 137 (2017) 65–78, https://doi.org/10.1016/j.ijleo.2017.02.060.

[8] J.L. Bartlett, X. Li, An overview of residual stresses in metal powder bed fusion, Addit. Manuf. 27 (2019) 131–149, https://doi.org/10.1016/j.addma.2019.02.020.

[9] J.D. Roehling, W.L. Smith, T.T. Roehling, B. Vrancken, G.M. Guss, J.T. McKeown, M.R. Hill, M.J. Matthews, Reducing residual stress by selective large-area diode surface heating during laser powder bed fusion additive manufacturing, Addit. Manuf. 28 (2019) 228–235, https://doi.org/10.1016/j.addma.2019.05.009.

[10] L. Zhuo, Z. Wang, H. Zhang, E. Yin, Y. Wang, T. Xu, C. Li, Effect of post-process heat treatment on microstructure and properties of selective laser melted AlSi10Mg alloy, Mater. Lett. 234 (2019) 196–200, https://doi.org/10.1016/j.matlet.2018.09.109.

[11] E. Beevers, A.D. Brandão, J. Gumpinger, M. Gschweitl, C. Seyfert, P. Hofbauer, T. Rohr, T. Ghidini, Fatigue properties and material characteristics of additively manufactured AlSi10Mg – effect of the contour parameter on the microstructure, density, residual stress, roughness and mechanical properties, Int. J. Fatigue 117 (2018) 148–162, https://doi.org/10.1016/j.ijfatigue.2018.08.023.

[12] C. López, A. Elías-Zúñiga, I. Jiménez, O. Martínez-Romero, H.R. Siller, J.M. Diabb, Experimental determination of residual stresses generated by single point incremental forming of AlSi10Mg Sheets produced using SLM additive manufacturing process, Materials (Basel). 11 (2018). doi:https://doi.org/10.3390/ma11122542.

[13] P. Yang, M.A. Rodriguez, L.A. Deibler, B.H. Jared, J. Griego, A. Kilgo, A. Allen, D.K. Stefan, Effect of thermal annealing on microstructure evolution and mechanical behavior of an additive manufactured AlSi10Mg part, J. Mater. Res. 33 (2018) 1701–1712, https://doi.org/10.1557/jmr.2018.82.

[14] J.R. Hönnige, P.A. Colegrove, S. Ganguly, E. Eimer, S. Kabra, S. Williams, Control of residual stress and distortion in aluminium wire + arc additive manufacture with rolling, Addit. Manuf. 22 (2018) 775–783, https://doi.org/10.1016/j.addma.2018.06.015.

[15] G. Piscopo, E. Atzeni, F. Calignano, M. Galati, L. Iuliano, P. Minetola, A. Salmi, Machining induced residual stresses in AlSi10Mg component produced by laser powder bed fusion (L-PBF), Procedia CIRP. 79 (2019) 101–106, https://doi.org/10.1016/j.procir.2019.02.019.

[16] M.F. Zaeh, G. Branner, Investigations on residual stresses and deformations in selective laser melting, Prod. Eng. Res. Dev. 4 (2010) 35–45, https://doi.org/10.1007/s11740-009-0192-y.

[17] X. Xing, X. Duan, X. Sun, H. Gong, L. Wang, F. Jiang, Modification of residual stresses in laser additive manufactured AlSi10Mg specimens using an ultrasonic peening technique, Materials (Basel). 12 (2019). doi:https://doi.org/10.3390/ma12030455.
[18] A. Salmi, E. Atzeni, Residual stress analysis of thin AlSi10Mg parts produced by laser powder bed fusion, Virtual Phys. Prototyp. 15 (2020) 49–61, https://doi.org/10.1080/17452759.2019.1650237.
[19] C. Colombo, C.A. Biffi, J. Fiocchi, D. Scaccabarozzi, B. Saggin, A. Tuissi, L.M. Vergani, Modulating the damping capacity of SLMed AlSi10Mg trough stress-relieving thermal treatments, Theor. Appl. Fract. Mech. 107 (2020) 1–6, https://doi.org/10.1016/j.tafmec.2020.102537.
[20] L. Wang, X. Jiang, Y. Zhu, Z. Ding, X. Zhu, J. Sun, B. Yan, Investigation of performance and residual stress generation of AlSi10Mg processed by selective laser melting, Adv. Mater. Sci. Eng. 2018 (2018) https://doi.org/10.1155/2018/7814039.
[21] C.A. Brice, W.H. Hofmeister, Determination of bulk residual stresses in electron beam additive-manufactured aluminum, Metall. Mater. Trans. A Phys. Metall. Mater. Sci. 44 (2013) 5147–5153, https://doi.org/10.1007/s11661-013-1847-z.
[22] A. Hussein, L. Hao, C. Yan, R. Everson, Finite element simulation of the temperature and stress fields in single layers built without-support in selective laser melting, Mater. Des. 52 (2013) 638–647, https://doi.org/10.1016/j.matdes.2013.05.070.
[23] W. Shifeng, L. Shuai, W. Qingsong, C. Yan, Z. Sheng, S. Yusheng, Effect of molten pool boundaries on the mechanical properties of selective laser melting parts, J. Mater. Process. Technol. 214 (2014) 2660–2667, https://doi.org/10.1016/j.jmatprotec.2014.06.002.
[24] P. Vora, K. Mumtaz, I. Todd, N. Hopkinson, AlSi12 in-situ alloy formation and residual stress reduction using anchorless selective laser melting, Addit. Manuf. 7 (2015) 12–19, https://doi.org/10.1016/j.addma.2015.06.003.
[25] B. Cheng, S. Shrestha, K. Chou, Stress and deformation evaluations of scanning strategy effect in selective laser melting, Addit. Manuf. 12 (2016) 240–251, https://doi.org/10.1016/j.addma.2016.05.007.
[26] D.-K. Kim, W. Woo, J.-H. Hwang, K. An, S.-H. Choi, Stress partitioning behavior of an AlSi10Mg alloy produced by selective laser melting during tensile deformation using in situ neutron diffraction, J. Alloys Compd. 686 (2016) 281–286, https://doi.org/10.1016/j.jallcom.2016.06.011.
[27] D. Dai, D. Gu, R. Poprawe, M. Xia, Influence of additive multilayer feature on thermodynamics, stress and microstructure development during laser 3D printing of aluminum-based material, Sci. Bull. 62 (2017) 779–787, https://doi.org/10.1016/j.scib.2017.05.007.
[28] L.S. Schadler, C. Galiotis, Fundamentals and applications of micro Raman spectroscopy to strain measurements in fibre reinforced composites, Int. Mater. Rev. 40 (1995) 116–134.
[29] I. De Wolf, Micro-Raman spectroscopy to study local mechanical stress in silicon integrated circuits, Semicond. Sci. Technol. 11 (1995) 139–154.
[30] S.J. Harris, A. O'Neill, J. Boileau, W. Donlon, X. Su, B.S. Majumdar, Application of the Raman technique to measure stress states in individual Si particles in a cast Al-Si alloy, Acta Mater. 55 (2007) 1681–1693, https://doi.org/10.1016/j.actamat.2006.10.028.
[31] S. Joseph, S. Kumar, V.S. Bhadram, C. Narayana, Stress states in individual Si particles of a cast Al-Si alloy: micro-Raman analysis and microstructure based modeling, J. Alloys Compd. 625 (2015) 296–308, https://doi.org/10.1016/j.jallcom.2014.10.207.
[32] W. Qiu, C.L. Cheng, R.R. Liang, C.W. Zhao, Z.K. Lei, Y.C. Zhao, L.L. Ma, J. Xu, H.J. Fang, Y.L. Kang, Measurement of residual stress in a multi-layer semiconductor heterostructure by micro-Raman spectroscopy, Acta Mech. Sinica 32 (2016) 805–812, https://doi.org/10.1007/s10409-016-0591-1.
[33] P. Jannotti, G. Subhash, J. Zheng, V. Halls, Measurement of microscale residual stresses in multi-phase ceramic composites using Raman spectroscopy, Acta Mater. 129 (2017) 482–491, https://doi.org/10.1016/j.actamat.2017.03.015.
[34] E. Anastassakis, A. Pinczuk, E. Burstein, F.H. Pollak, M. Cardona, Effect of static uniaxial stress on the Raman spectrum of silicon, Solid State Commun. 8 (1970) 133–138.
[35] E. Anastassakis, E. Liarokapis, Polycrystalline Si under strain: elastic and lattice-dynamical considerations, J. Appl. Phys. 62 (1987) 3346–3352, https://doi.org/10.1063/1.339296.
[36] E. Anastassakis, A. Cantarero, M. Cardona, Piezo-Raman measurements and anharmonic parameters in silicon and diamond, Phys. Rev. B 41 (1990) 7529–7535, https://doi.org/10.1103/PhysRevB.41.7529.
[37] X.P. Li, X.J. Wang, M. Saunders, A. Suvorova, L.C. Zhang, Y.J. Liu, M.H. Fang, Z.H. Huang, T.B. Sercombe, A selective laser melting and solution heat treatment refined Al-12Si alloy with a controllable ultrafine eutectic microstructure and 25% tensile ductility, Acta Mater. 95 (2015) 74–82, https://doi.org/10.1016/j.actamat.2015.05.017.
[38] Z. Iqbal, S. Veprek, A.P. Webb, P. Capezzuto, Raman scattering from small particle size polycrystalline silicon, Solid State Commun. 37 (1981) 993–996. doi:DOI: https://doi.org/10.1016/0038-1098(81)91202-3.
[39] Y. Kanemitsu, H. Uto, Y. Masumoto, T. Matsumoto, T. Futagi, H. Mimura, Microstructure and optical properties of free standing porous silicon films: size dependence of absorption spectra in Si nanometer-sized crystallites, Phys. Rev. B 48 (1993) 2827–2831.
[40] A.P. Meilakhs, S.V. Koniakhin, New explanation of Raman peak redshift in nanoparticles, Superlattice. Microst. 110 (2017) 319–323, https://doi.org/10.1016/j.spmi.2017.08.010.
[41] Y. Gao, P. Yin, Origin of asymmetric broadening of Raman peak profiles in Si nanocrystals, Sci. Rep. 7 (2017) 43602, https://doi.org/10.1038/srep43602.
[42] J. Zi, H. Büscher, C. Falter, W. Ludwig, K. Zhang, X. Xie, Raman shifts in Si nanocrystals, Appl. Phys. Lett. 69 (1996) 200–202, https://doi.org/10.1063/1.117371.
[43] C. Ossadnik, S. Vepřek, I. Gregora, Applicability of Raman scattering for the characterization of nanocrystalline silicon, Thin Solid Films 337 (1999) 148–151, https://doi.org/10.1016/S0040-6090(98)01175-4.
[44] M.N. Islam, S. Kumar, Influence of crystallite size distribution on the micro-Raman analysis of porous Si, Appl. Phys. Lett. 78 (2001) 715–717, https://doi.org/10.1063/1.1343494.
[45] G. Faraci, S. Gibilisco, P. Russo, A.R. Pennisi, S. La Rosa, Modified Raman confinement model for Si nanocrystals, Phys. Rev. B - Condens. Matter Mater. Phys. 73 (2006) 1–4, https://doi.org/10.1103/PhysRevB.73.033307.
[46] G. Irmer, Raman scattering of nanoporous semiconductors, J. Raman Spectrosc. 38 (2007) 634–646, https://doi.org/10.1002/jrs.1703.
[47] P. Alfaro, R. Cisneros, M. Bizarro, M. Cruz-Irisson, C. Wang, Raman scattering by confined optical phonons in Si and Ge nanostructures, Nanoscale. 3 (2011) 1246–1251, https://doi.org/10.1039/c0nr00623h.
[48] G. Amato, Sructural and Electrophysical Properties of Porous Silicon, in: G.S. Korotchenkov (Ed.), Porous Silicon From Form. to Appl., CRC Press, 2016: pp. 155–185.
[49] E.I. Ageev, D.V. Potorochin, D.V. Sachenko, G.V. Odintsova, Generation of web-like structures and nanoparticles by femtosecond laser ablation of silicon target in ambient air, Opt. Quant. Electron. 49 (2017) 40, https://doi.org/10.1007/s11082-016-0875-5.
[50] I.H. Campbell, P.M. Fauchet, The effects of microcrystal size and shape on the one phonon Raman spectra of crystalline semiconductors, Solid State Commun. 58 (1986) 739–741.
[51] S. Marola, D. Manfredi, G. Fiore, M.G. Poletti, M. Lombardi, P. Fino, L. Battezzati, A comparison of selective laser melting with bulk rapid solidification of AlSi10Mg alloy, J. Alloys Compd. 742 (2018) 271–279, https://doi.org/10.1016/j.jallcom.2018.01.309.
[52] F. Calignano, G. Cattano, D. Manfredi, Manufacturing of thin wall structures in AlSi10Mg alloy by laser powder bed fusion through process parameters, J. Mater. Process. Technol. 255 (2018) 773–783, https://doi.org/10.1016/j.jmatprotec.2018.01.029.
[53] H. Richter, Z.P. Wang, L. Ley, The one phonon Raman spectrum in microcrystalline silicon, Solid State Commun. 39 (1981) 625–629, https://doi.org/10.1016/0038-1098(81)90337-9.
[54] N. Brunetto, G. Amato, A new line shape analysis of Raman emission in porous silicon, Thin Solid Films 297 (1997) 122–124, https://doi.org/10.1016/S0040-6090(96)09363-7.
[55] B.D. Cullity, Elements of X-Ray Diffraction, Addison-Wesley Publishing Company, Boston, Massachussetts, U.S.A., 1956
[56] G.K. Williamson, W.H. Hall, X-ray line broadening from filed Aluminium and Wolfram, Acta Metall. 1 (1953) 22–31, https://doi.org/10.1016/0001-6160(53)90006-6.
[57] V.D. Mote, Y. Purushotham, B.N. Dole, Williamson-Hall analysis in estimation of lattice strain in nanometer-sized ZnO particles, J. Theor. Appl. Phys. 6 (2012). doi: https://doi.org/10.1186/2251-7235-6-6.
[58] A. Guagliardi, N. Masciocchi, Analisi di Materiali Policristallini Mediante Tecniche di Diffrazione, Insubria University Press, Varese, 2007.
[59] I. Yamauchi, K. Takahara, T. Tanaka, K. Matsubara, Chemical leaching of rapidly solidified Al-Si binary alloys, J. Alloys Compd. 396 (2005) 302–308, https://doi.org/10.1016/j.jallcom.2005.01.006.
[60] H. Qin, Q. Dong, V. Fallah, M.R. Daymond, Rapid solidification and non-equilibrium phase constitution in laser powder bed fusion (LPBF) of AlSi10Mg alloy: analysis of Nano-precipitates, eutectic phases, and hardness evolution, Metall. Mater. Trans. A Phys. Metall. Mater. Sci. 51 (2020) 448–466, https://doi.org/10.1007/s11661-019-05505-5.
[61] L. Thijs, K. Kempen, J.P. Kruth, J. Van Humbeeck, Fine-structured aluminium products with controllable texture by selective laser melting of pre-alloyed AlSi10Mg powder, Acta Mater. 61 (2013) 1809–1819, https://doi.org/10.1016/j.actamat.2012.11.052.
[62] J. Wu, X.Q. Wang, W. Wang, M.M. Attallah, M.H. Loretto, Microstructure and strength of selectively laser melted AlSi10Mg, Acta Mater. 117 (2016) 311–320, https://doi.org/10.1016/j.actamat.2016.07.012.
[63] D.-K. Kim, J.-H. Hwang, E.-Y. Kim, Y.-U. Heo, W. Woo, S.-H. Choi, Evaluation of the stress-strain relationship of constituent phases in AlSi10Mg alloy produced by selective laser melting using crystal plasticity FEM, J. Alloys Compd. 714 (2017) 687–697, https://doi.org/10.1016/j.jallcom.2017.04.264.
[64] X. Liu, C. Zhao, X. Zhou, Z. Shen, W. Liu, Microstructure of selective laser melted AlSi10Mg alloy, Mater. Des. 168 (2019) 107677, https://doi.org/10.1016/j.matdes.2019.107677.
[65] N. Takata, H. Kodaira, K. Sekizawa, A. Suzuki, M. Kobashi, Change in microstructure of selectively laser melted AlSi10Mg alloy with heat treatments, Mater. Sci. Eng. A 704 (2017) 218–228, https://doi.org/10.1016/j.msea.2017.08.029.
[66] C. Zhang, H. Zhu, Z. Hu, L. Zhang, X. Zeng, A comparative study on single-laser and multi-laser selective laser melting AlSi10Mg: defects, microstructure and mechanical properties, Mater. Sci. Eng. A 746 (2019) 416–423, https://doi.org/10.1016/j.msea.2019.01.024.
[67] J.R. Davis, Metals Handbook, Second Edi, ASM International, 1998.
[68] D.A. Porter, K.E. Easterling, M.Y. Sherif, Phase Transormations in Metals and Alloys, Third Edit, CRC Press, Taylor & Francis group, Boca Raton, FL, U.S.A., 2009